ACS OMEGA

Open Access

http://pubs.acs.org/journal/acsodf

Article

Collective and Coordinated Conformational Changes Determine Agonism or Antagonism at the Human Trace Amine-Associated Receptor 1

Agustín I. Robles, Luis Dinamarca-Villarroel, Gonzalo E. Torres, and Angélica Fierro*

Cite This: *ACS Omega* 2023, 8, 43051−43059

Read Online

ACCESS | Metrics & More | Article Recommendations | Supporting Information

ABSTRACT: The human trace amine-associated receptor (hTAAR1), a G protein-coupled receptor, has been postulated as a new target in the treatment of neuropsychiatric conditions. The mechanism associated with activation or inactivation by agonists or antagonists in hTAAR1 and other GPCRs has not yet been fully elucidated. In this study, we combined computational methods including homology modeling, docking, and molecular dynamic simulations to reveal novel conformational changes associated with agonist and antagonist interactions in hTAAR1. Our findings suggest a differential cascade of coordinated movements based on the presence of either an agonist or antagonist and primarily involving the second extracellular loop, transmembrane domain 5, and the third intracellular domains of hTAAR1. Our study provides an opportunity to predict the effects on new ligands with agonistic or antagonistic activity at hTAAR1 based on the reported conformational changes.

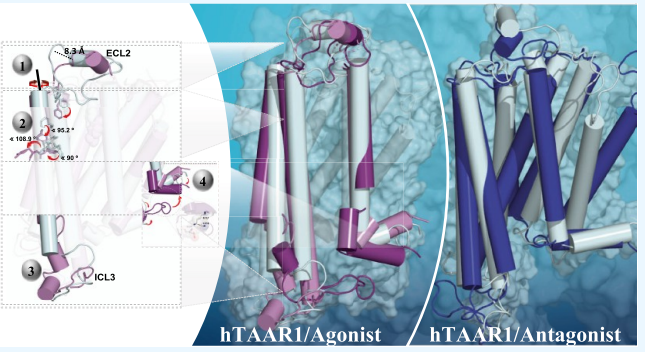

INTRODUCTION

In the last decades, biomedical research has been revolutionized by the application of computational approaches for the identification of new therapeutic targets and the design of novel compounds with biological activity.[1,2] Currently, the rationale for the design of drugs with potential therapeutic effects is focused on their affinity for the target protein binding cavity and their ability to mimic the molecular interactions promoted by endogenous ligands. However, the design of new chemical structures with specific binding cavity interactions, referred to as pharmacophores,[3,4] presents some important limitations. In the case of G protein-coupled receptors (GPCRs), the interaction of agonists or antagonists with the receptor binding cavity is only the first step in a series of molecular events that include additional conformational changes within the protein. The information gained from the additional cascade of conformational movements can provide new opportunities in drug discovery research.[5,6]

Previous studies have shown that the transmembrane domains (TMDs) of GPCRs undergo different specific movements depending on whether the receptor binds to an agonist or an antagonist.[7] One of the limitations of those studies is the lack of information regarding the contribution of extracellular and intracellular loops (ECL and ICL, respectively) that link TMDs. ECLs play an important role in the interaction between receptors and ligands, while ICLs appear to be more important for the interactions with G proteins.[8−10] A comprehensive understanding of all conformational changes induced by receptor ligands in a specific GPCR could be used as a model to predict the types of movements generated by an agonist or antagonist in additional GPCRs using computational tools.

The human trace amine-associated receptor-1 (hTAAR1) was identified two decades ago,[11] and several recent studies have suggested that this receptor is an important target for neuropsychiatric diseases.[12] Previous studies have shown distinct conformational changes associated with TAAR1 in different species (human and mouse) in the presence of an antagonist with high affinity for the mouse receptor (mTAAR1).[13] However, the structural information associated with hTAAR1 is limited. Indeed, no specific interactions have been studied for hTAAR1 complexed with agonists. Thus, we asked whether agonists and antagonists produce different conformational changes in hTAAR1 and whether this information could help us to understand pharmacological activity. Because the crystal structure of hTAAR1 is not available, a computational model was generated based on the

Received: August 24, 2023
Revised: October 13, 2023
Accepted: October 17, 2023
Published: October 31, 2023

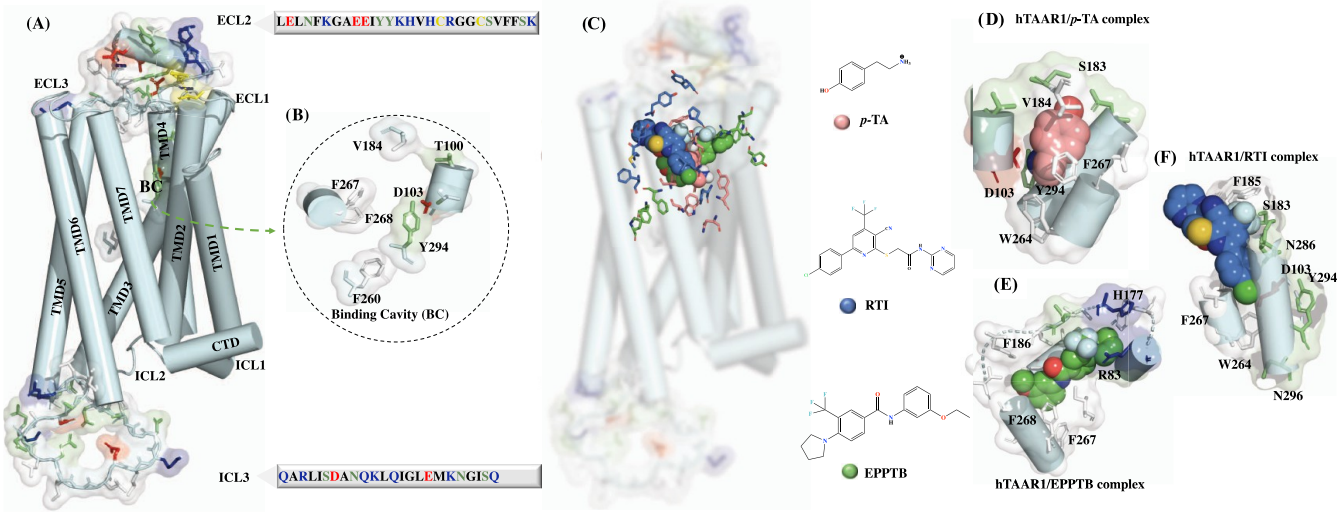

Figure 1. Structure of hTAAR1 and main interactions with *p*-TA, EPPTB, and RTI. (A) Model of the three-dimensional structure of hTAAR1 is shown in polar blue, highlighting the sequence of ECL2 (top) and ICL3 (bottom). (B) Residues that form part of the BC. (C) Superimposed image of agonist and antagonists into the hTAAR1 cavity with their chemical structures are displayed. (D−F) hTAAR1 complexes interacting with *p*-TA (peach), EPPTB (green), and RTI (blue), respectively. Residues contributing to the electrostatic surfaces are shown in color (nonpolar residues are white, polar uncharged are green, negatively charged are red, and positively charged are blue).

crystal structure of the closely related β2-adrenergic receptor (β2AR).[14] Here, we modeled the entire hTAAR1 coding sequence, including intracellular and extracellular loops in the absence and in the presence of the agonist *p*-tyramine (4-hydroxyphenylethylamine (*p*-TA)) and two antagonists of TAAR1 described to date, *N*-(3-ethoxyphenyl)-4-pyrrolidin-1-yl-3-trifluoromethylbenzamide (EPPTB)[15] having high affinity for mTAAR1, and 2-[[6-(4-chlorophenyl)-3-cyano-4-(trifluoromethyl)-2-pyridinyl]thio]-*N*-2-pyrimidinylacetamide (RTI-7470−44, hereinafter RTI), a more recent antagonist having higher affinity for hTAAR1.[16] The receptor−ligand complexes were submitted to molecular dynamics, and a detailed analysis of their conformational movements was performed using distance correlation maps. Our findings suggest a coordinated movement based on the presence of an agonist involving the second extracellular loop, transmembrane domain 5, and the third intracellular domains of hTAAR1. Here, we provide structural information associated with conformational changes induced by agonists or antagonists within hTAAR1. We also describe the binding cavity for RTI-7470−44 and its main interactions. This information could be used to predict the pharmacological effect of the molecules at GPCRs.

RESULTS AND DISCUSSION

Three-Dimensional Structure of hTAAR1 and Its Interaction with *p*-TA and Antagonists. To generate new structural and mechanistic insights of hTAAR1, we built a model using the β2AR (PDBid: 2RH1[17]) as a template. Figure 1A shows the overall structure of hTAAR1 with seven helixes representing TMDs connected by three ICLs and three ECLs. ICL3 (residues 220-243) and ECL2 (residues 161-188) containing primarily charged polar residues (in licorice blue, red, and green) are highlighted since previous studies have described their important contribution to human and mouse TAAR1/EPPTB complexes.[13] Figure 1B shows the binding cavity formed by D103, F260, F267, F268, and Y294, depicting a electron-rich environment where ligands could be accommodated and stabilized. A superimposed image of the agonist and antagonists and the residues closest to the hTAAR1 binding cavity is displayed in Figure 1C. In Figure 1D−F, a partial fragment of the binding cavity and main interactions are displayed for each complex.

Electron-Rich Environment Accommodates EPPTB, RTI, and *p*-TA in hTAAR1 during the Simulation. After docking analysis, the hTAAR1/*p*-TA, hTAAR1/EPPTB, and hTAAR1/RTI complexes were inserted into a lipid membrane and solvated in a water box to perform molecular dynamics (MD) simulations of 1500 ns. Specific interactions observed from docking studies remained throughout the simulation. As shown in Figure 2, three representative frames of the MD analysis depict hTAAR1/EPPTB, hTAAR1/RTI, and hTAAR1/*p*-TA during simulation. In Figure 2A−C, the hTAAR1/EPPTB complex at 1, 300, and 1500 ns shows that EPPTB is buried in the cavity as a consequence of a displacement of 5.5 Å inside the receptor at 300 ns. The final complex at 1500 ns shows interactions between the antagonist and the receptor through aromatic residues including F186, F195, F267, F268, and W264. The overall analysis shows a RMSD value of approximately 7 Å for the entire receptor (<3 Å for the protein without ICL3) and the main shift in RMSF was observed from residues 220 to 243 (ICL3) and 161 to 188 (ECL2) (see Figure S1A−C).

To gain new structural insights into hTAAR1 antagonism, we conducted the initial structural analysis of RTI, a potent antagonist of hTAAR1 recently described by Decker and colleagues.[16] To pinpoint the binding cavity of RTI on hTAAR1, we initially explored potential BCs, identifying two primary interaction sites (Figure S2). One corresponds to the binding cavity for *p*-TA, while the second aligns with the site previously described for EPPTB.[13] Considering the volume and structural characteristics of the RTI, we utilized the second cavity to assess the most stable pose within the hTAAR1 cavity (Figure 2D).

Following molecular docking studies, we conducted a molecular dynamics simulation. In Figure 2D−E, the principal interactions of RTI within the binding cavity during the simulation reveal a highly aromatic cavity (Y172, F185, F195, F267, Y279, and F292), with charged and polar residues such

https://doi.org/10.1021/acsomega.3c06315
ACS Omega 2023, 8, 43051−43059

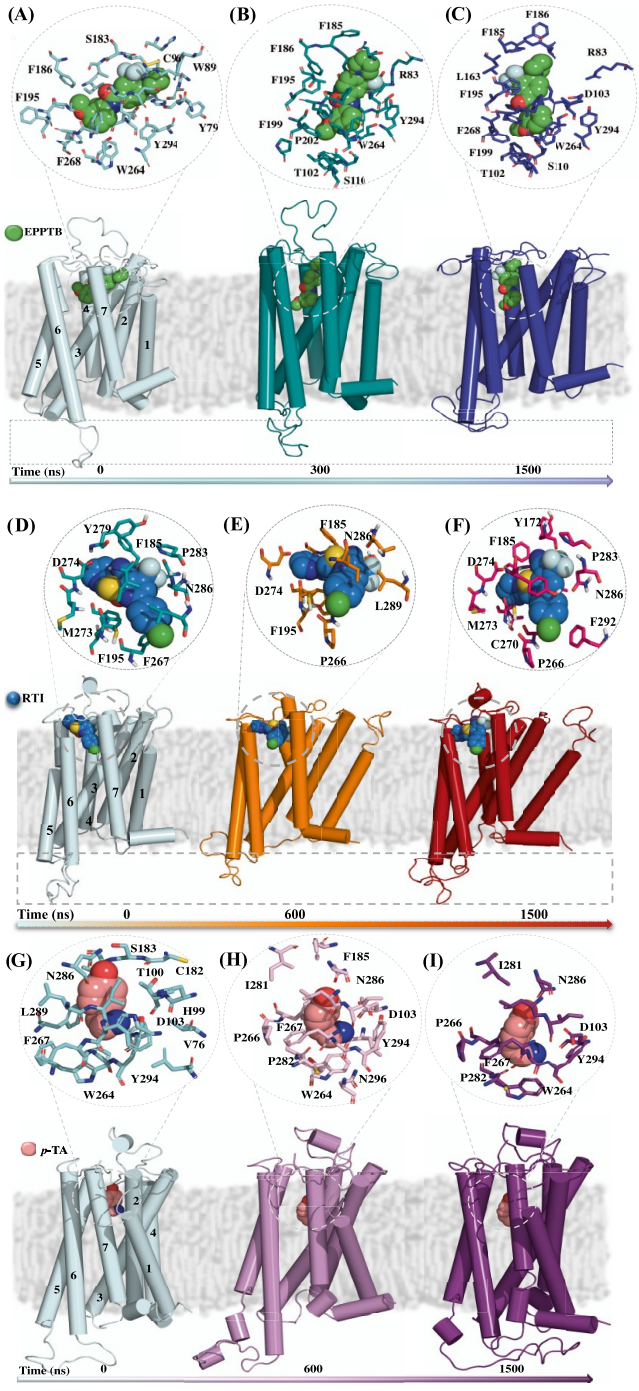

Figure 2. Molecular dynamics of hTAAR1 with EPPTB (A−C), RTI (D−F), and *p*-TA (G-I) for 1500 ns. Three-dimensional model of hTAAR1 at 1 ns (polar blue). A slice representation of the main interactions between hTAAR1 residues and ligands at 5 Å is shown in top panels. Scale colors from polar blue to blue, red, and purple describe the molecular dynamics for EPPTB, RTI, and *p*-TA, respectively.

as D274 and N286 contributing to ligand stabilization. The chlorine atom engages in interactions with F292 and P266. Our analysis describes the stability of this system over 1500 ns (refer to Figure S3), where ICL3 interacts with ICL2 (Figure S3).

Our computational findings replicate the observed conformational changes in the hTAAR1/EPPTB complex moving ICL3 away from the carboxy-terminal domain (Figure 2C,2F). Both antagonists are significantly stabilized by aromatic residues. Although the surroundings are not identical, F185 and F186 stabilize the CF3 group and the aromatic center for EPPTB and RTI, approximately, at 4 and 6 Å distances, respectively.

The hTAAR1/*p*-TA complex primarily involves polar residues and remains stable during the simulation (RMSD around 6 Å for the entire receptor and <3 Å for the protein without ICL3, Figure S4A,B). Three representative frames at 1, 600, and 1500 ns show a hydrogen bond interaction of *p*-TA with N286, a coulombic interaction with D103, and a hydrogen bond with S107 through the simulation (Figure 2G−I). The aromatic residues that form the cavity contribute to an electronic environment during simulation. Toward the simulation's conclusion, the more stable conformation of *p*-TA results in both the agonist and antagonists sharing a common binding site (*p*-TA displacement measures 4−5 Å, as depicted in Figure S2B). However, a conformational change of ICL3 at 900 ns was observed. The distance from the ICL3 domain to the carboxy-terminal domain (CTD) decreased from 35 to 13 Å (Figure 3A−C). Moreover, the angle formed by residues L215-Q222-P309 changed from 100 to 12° during the simulation (Figure S4C−D). Consequently, the polar interactions between ICL3 and the CTD were enhanced (Figure 3D). The solvent-accessible surface area (SASA) decreased, and the radius of gyration (Rg) indicated a more compact system (Figure S4E and S4F).

Agonist *p*-TA is Responsible for the Occlusion Movement of ICL3 in hTAAR1. To analyze whether *p*-TA induces conformational changes that favor an interaction between ICL3 and CTD and to verify that this is not an artifact, we repeated the receptor simulation in the absence of the ligand using coarse-grained (CG) MD for 5200 ns. Interestingly, the absence of *p*-TA in the cavity of hTAAR1 did not result in any movement of ICL3 toward CTD (Figure S5A). Furthermore, in the absence of the ligand, an opening of an intracellular cavity was observed, consistent with a receptor−G protein interaction in the absence of receptor activation[9] (Figure S5B). Therefore, our data demonstrate that ICL3 movement depends on the presence of the agonist.

Energetic Differences between hTAAR1/*p*-TA and hTAAR1/Antagonists. The substantial surface area of the molecular structure of the antagonists compared to *p*-TA allows for more aromatic interactions, consistent with the difference in free energy between EPPTB, RTI, and *p*-TA as calculated through MM-PBSA (Figure 4A). The energy distribution associated with the hTAAR1/*p*-TA system demonstrates a free energy of −4.42 kcal/mol, for the hTAAR1/EPPTB system, it is −12.39 kcal/mol, and for the hTAAR1/RTI system, it is −17.84 kcal/mol (Figure 4B,C). Interestingly, these results align with experimental findings, where RTI exhibits a greater affinity for hTAAR1 compared to EPPTB.[16]

The per-residue energy decomposition studies indicate that the free energy variation of hTAAR1 residues for EPPTB and RTI is significantly lower in magnitude than that of *p*-TA (Figure 4B−D). Based on the chemical structures at physiological pH, *p*-TA is protonated, creating a distinct difference between the agonist and antagonists under evaluation. As a result, the ammonium form of *p*-TA establishes coulombic interactions (charge-to-charge) with negatively charged amino acids, such as D69 and D103,

https://doi.org/10.1021/acsomega.3c06315
ACS Omega 2023, 8, 43051−43059

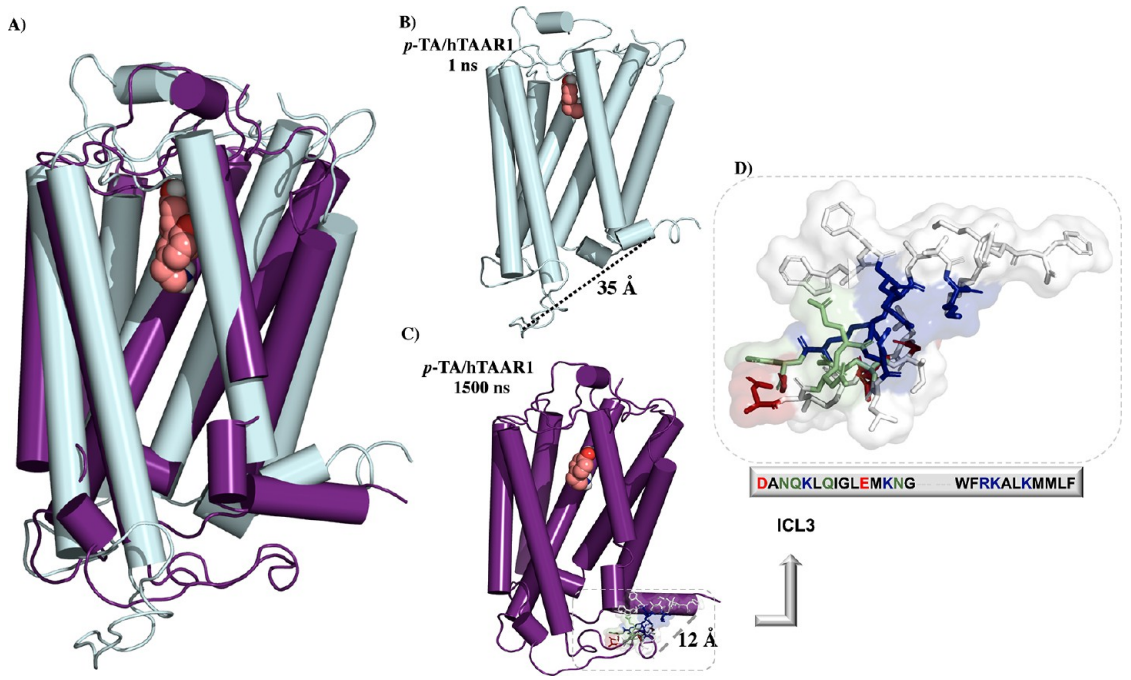

Figure 3. Conformational and electrostatic changes of the hTAAR1/*p*-TA complex. (A) superposition of hTAAR1/*p*-TA at 1 and 1500 ns. (B, C) Conformational movements of ICL3 at 1 and 1500 ns. (D) Alignment of the sequence of ICL3 with its conformational representation (on polar residues, the uncharged polar residues are white, the negatively charged residues are red, and the positively charged residues are blue).

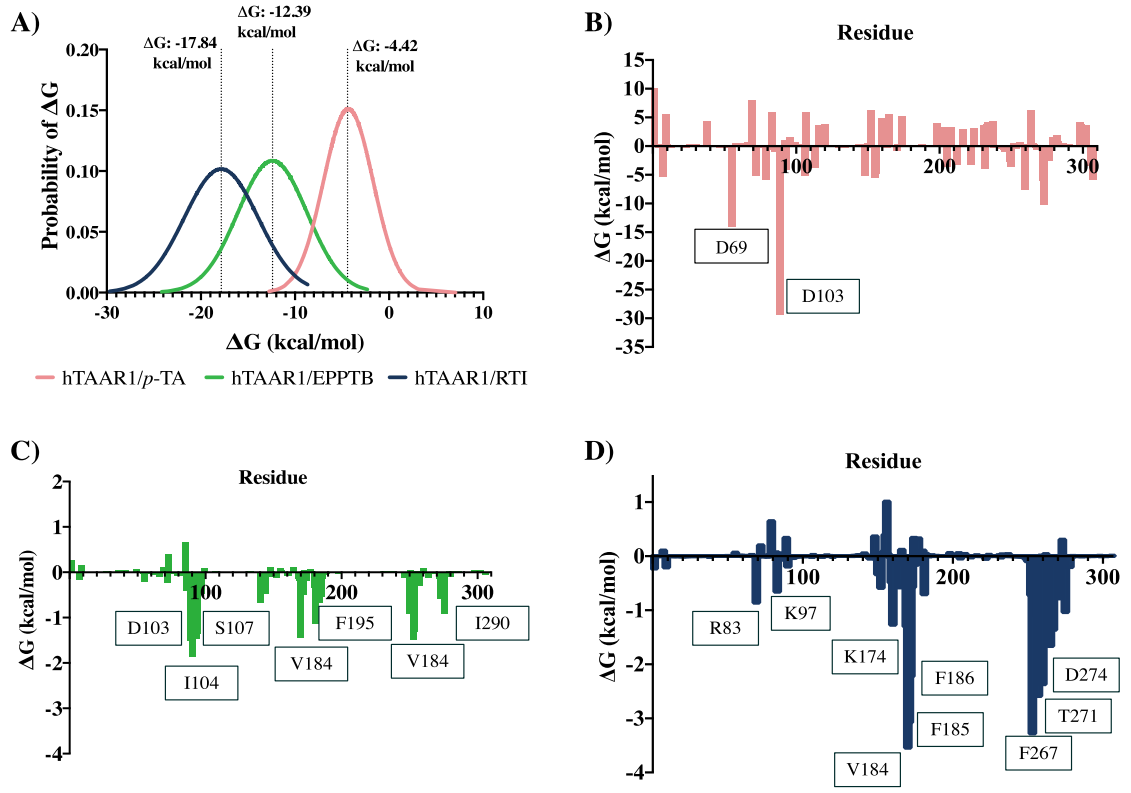

Figure 4. Comparison of energy analysis of hTAAR1/*p*-TA, hTAAR1/EPPTB, and hTAAR1/RTI complexes. (A) MM-PBSA for the hTAAR1/*p*-TA (peach), hTAAR1/EPPTB (green), and hTAAR1/RTI (blue) complexes. (B–D) Per-residue energy decomposition for the hTAAR1/*p*-TA, hTAAR1/EPPTB, and hTAAR1/RTI complexes.

contributing significantly with −15.5 and −20.3 kcal/mol, respectively, to stabilize the agonist during the simulation (see Figure 4B). While the dipole moment of *p*-TA is greater than that of EPPTB and RTI, the antagonists exhibit an extended charge distribution due to the presence of an extended π cloud and electron-rich heteroatoms such as fluorine and sulfur.

However, as described in Figure 4A, the hTAAR1/antagonist complexes are energetically more stable than the

https://doi.org/10.1021/acsomega.3c06315
ACS Omega 2023, 8, 43051−43059

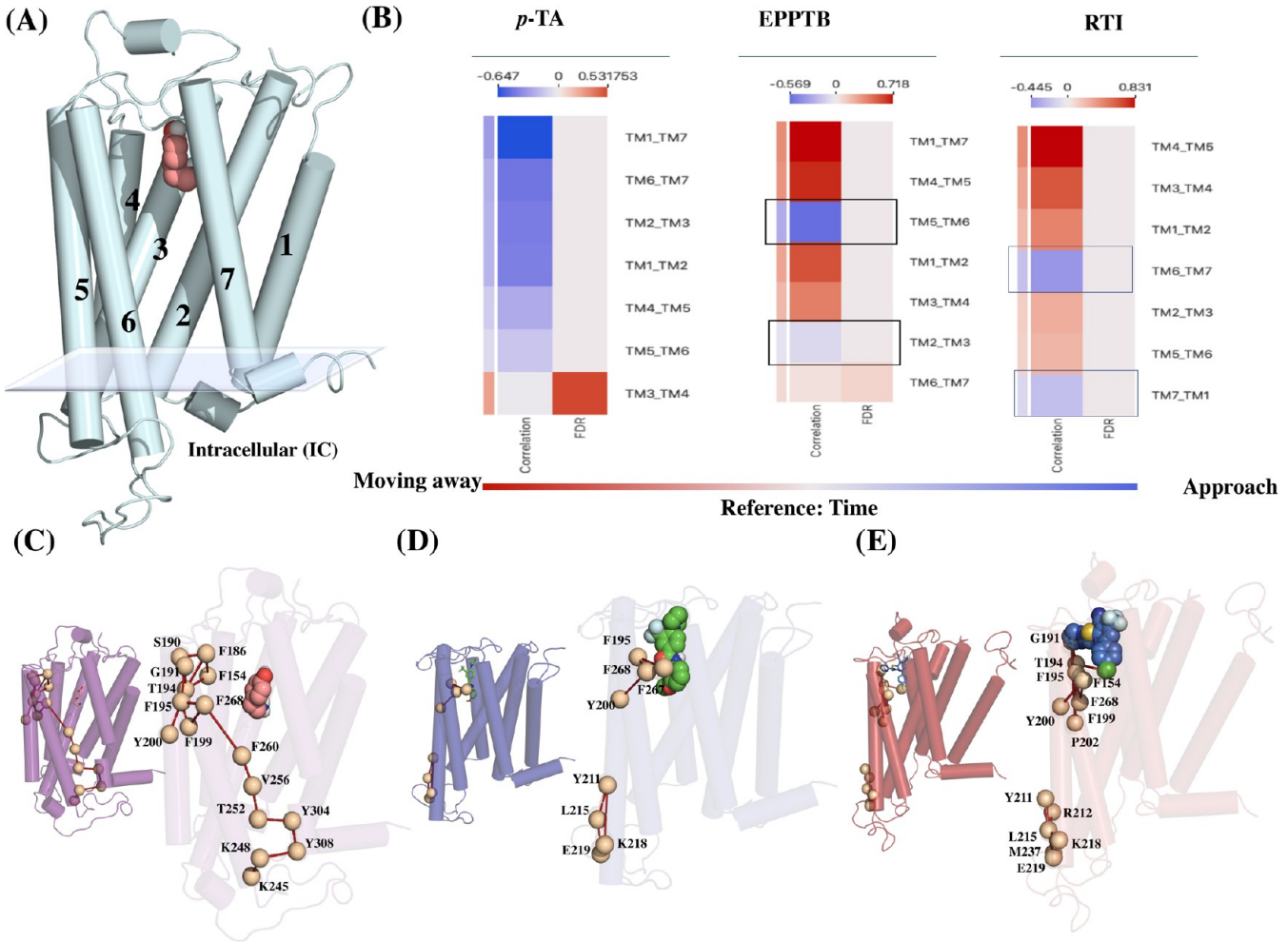

Figure 5. Analysis of structural and correlation movements for the hTAAR1/*p*-TA and hTAAR1/antagonist's systems. (A, B) Correlation map of the intracellular segment of hTAAR1/*p*-TA, hTAAR1/EPPTB, and hTAAR1/RTI complexes. (C−E) Interaction network of hTAAR1 in complex with *p*-TA, EPPTB, and RTI, respectively. The interaction network is represented for C-α (in spheres) of the main residues.

hTAAR1/*p*-TA complex (RTI around 13 kcal/mol better than that of *p*-tyramine), which can be attributed to the greater number of amino acids that disrupt the hTAAR1/*p*-TA interaction (yielding positive energy values). Furthermore, both EPPTB and RTI exhibit a combined effect of coulombic and van der Waals interactions, which can be attributed to molecular properties such as shape, size, and the electronic distribution of their respective structures, when compared to *p*-TA. Consequently, aromatic residues such as F185, F186, and F267 as well as charged residues such as R83, K97, and K174 among others play a role in accommodating ligands within the cavity and continue to interact during the simulation.

TMD Movement Differentiates between Agonism and Antagonism. To elucidate the collective interactions within hTAAR1 in the presence of an agonist or antagonist, we examined the overall collective motions in the transmembrane domains (TMDs) to uncover potential movement patterns linked to either agonist or antagonist binding in hTAAR1. Correlation heat maps were utilized to assess variations in the distance relationships between TMDs over the course of the MD simulations. A positive correlation value indicates that the distance between the domains increases as the simulation progresses, while a negative value corresponds to a decrease in the distance over time.

Further analysis of the correlation maps shows that all TMDs approach each other in the presence of *p*-TA (Figure 5A,B, depicted in blue), aligning with the ICL3−CTD interaction described earlier. Conversely, TMDs 2 and 3, along with TMDs 5 and 6, exhibit convergence in the presence of EPPTB. Moreover, TMDs 6 and 7 as well as TMDs 7 and 1 demonstrate closer proximity to one another in the presence of RTI, while the remaining TMD pairs move apart from each other (depicted in red in Figure 5B).

Our analysis of the correlation maps indicates that in the presence of an agonist, the TMDs adopt a shot glass-shaped bundle structure, resulting in a reduction of the intracellular distance between them. Conversely, in the presence of an antagonist, the TMDs move apart from each other within the intracellular plane. Drawing from this observation, we conducted a study of protein interaction networks for the various complexes under investigation, aiming to provide insights into the distinct conformational responses between agonists and antagonists. *p*-TA initiates a network of interactions that originate from the aromatic amino acids within the binding cavity and extend to the intracellular portions of TMD5 and TMD6 (as illustrated in Figure 5C). Conversely, this interaction network is not observed with any of the antagonists (as depicted in Figure 5D−E). In the case of both antagonists, two primary interaction networks form: one

https://doi.org/10.1021/acsomega.3c06315
ACS Omega 2023, 8, 43051−43059

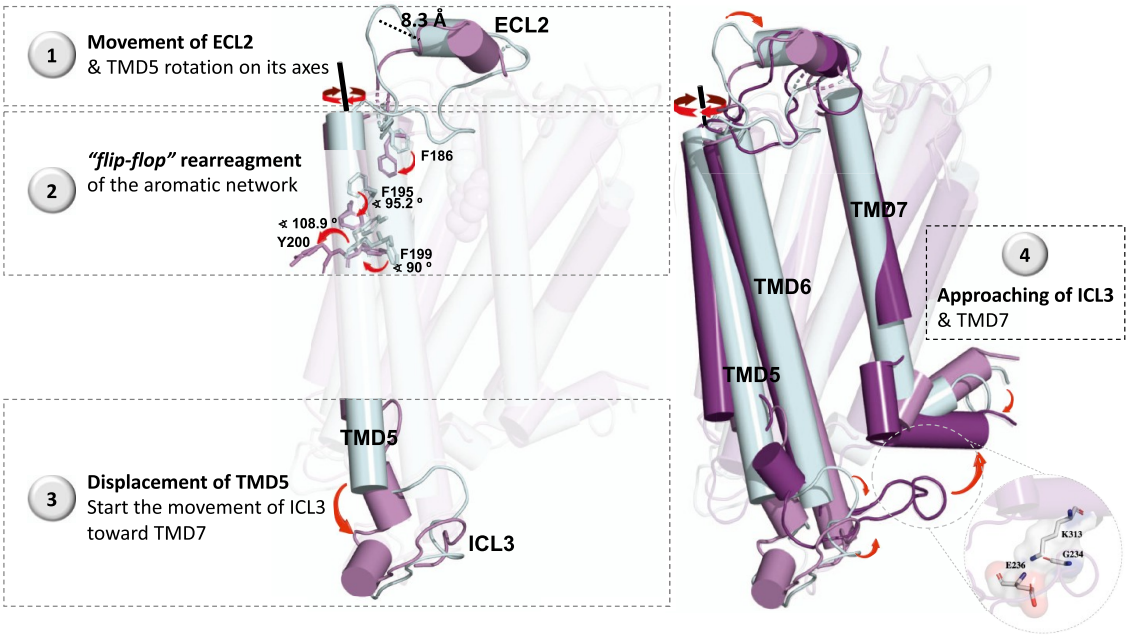

Figure 6. Conformational movements in hTAAR1 are associated with the presence of *p*-TA. 1, ECL2 displacement at 1 ns and 600 ns. 2, Aromatic residue *flip-flop* movement at 1 and 600 ns. 3, ICL3 movement at 1 and 600 ns. 4, Movement of TMD7 at 1, 600, and 1500 ns. hTAAR1 at 1, 600, and 1500 ns are represented in polar blue, lilac, and purple, respectively.

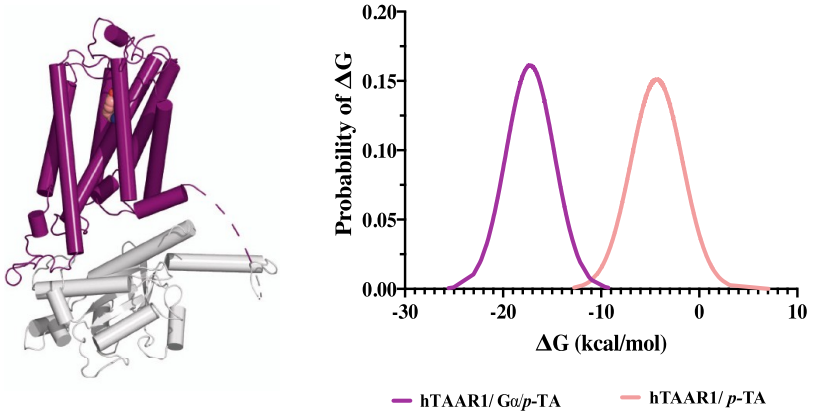

Figure 7. G protein stabilizes the hTAAR/*p*-TA complex. Normal distribution of MM-PBSA for the hTAAR/*p*-TA (peach) and hTAAR1/Gα/*p*-TA (purple). Gα is shown in cartoon white.

in proximity to the binding cavity and the other within the designated intracellular segment. Furthermore, we note that RTI exhibits a more extensive network of aromatic interactions compared to EPPTB, signifying a distinction between the two antagonists. A comprehensive view of the interaction network is shown in Figure S6.

"*Domino Effect*" Caused by ECL2 in hTAAR1. The main conclusion drawn from our study is that the movement of ICL3 potentially serves as an indicator of the activity of agonists or antagonists in hTAAR1. To explain the ICL3's conformational changes induced by the agonist, we propose a model outlining a sequence of orchestrated movements through the following steps (Figure 6): (1) Loss of ECL2/*p*-TA interactions: The aromatic ring of *p*-TA interacts with V184 from ECL2 and H99 from TMD3. Once *p*-TA is accommodated into the cavity, these interactions are severed, leading to an approximate displacement of 8 Å. (2) "Flip-flop" movement: enhanced mobility in ECL2 permits TMD5 to rotate, resulting in π-complex formation facilitated by the movements of F195 and Y200. (3) Movement of ICL3: the stabilization of TMD5 leads to an expansion in the movement of ICL3 toward CTD (see Figure 3C). (4) Movement of TMD7: finally, TMD7 moves closer to TMD6 on the intracellular side, thereby facilitating the interaction of ICL3 with TMD7 (illustrated in step 4 in Figure 6) through the involvement of residues E236 and G234 from ICL3 with K313 of TMD7. These findings suggest that the movement of ICL3 differs depending on the presence of an agonist or an antagonist, and the π-complex formation step emerges as pivotal in coordinating the sequence of movements involving ICL3-CTD.

Coordinated Conformational Change in hTAAR1 Generates a Transient Conformational State. Based on the energy data and the structural analysis, we have observed that the energy contribution for the range of amino acids corresponding to ICL3 (residues 215-245) and the terminal fragment of TMD7 (residues 311-314) is positive-valued. Consequently, we speculate that the movement of ICL3 could

https://doi.org/10.1021/acsomega.3c06315
ACS Omega 2023, 8, 43051−43059

signify a transient state toward receptor inactivation subsequent to Gs release. If this assumption is correct, the hTAAR1/*p*-TA system should be less stable compared to a system where the Gs protein is present. In order to test this new hypothesis, we conducted a coarse-grained molecular dynamic simulation spanning 5000 ns to ascertain whether Gs interacts with ICL3 and whether this interaction contributes to the stability of the hTAAR1/Gs complex. Our data indeed reveal that Gs interacts with ICL3 as well as with intracellular segments of several TMDs (as illustrated in Figure S7).

Finally, to validate the transient conformational state facilitated by the movement of ICL3, we conducted an all-atom molecular dynamic simulation of the hTAAR1/Gαs/*p*-TA complex during 300 ns. The energy of the hTAAR1/*p*-TA/Gαs system displays a considerably more negative value compared to the hTAAR1/*p*-TA system (−17.24 vs −4.42 kcal/mol, respectively). This observation aligns with a complex that demonstrates higher stability in the presence of Gα (as illustrated in Figure 7).

CONCLUSIONS

In this study, we employed *in silico* methodologies to generate a comprehensive 3D structural description of the hTAAR1 receptor complex. This encompassed 1500 ns of dynamics for the *p*-TA agonist, 1500 ns for the EPPTB antagonist, and 1500 ns of dynamics for the RTI antagonist. To evaluate the conformational changes occurring in the presence of *p*-TA, a coarse-grained system was utilized for 5200 ns in the absence of *p*-TA. Additionally, we assessed the impact of the complete Gs protein by means of coarse-grained simulations spanning 5000 ns. Furthermore, we aimed to explore how the presence of the G protein influences ligand stability, conducting a 300 ns molecular dynamics simulation with the Gα protein alongside the agonist (*p*-TA).

Our investigations unveiled the primary interactions of *p*-TA, EPPTB, and RTI within the hTAAR1 binding cavity. Employing various molecular dynamics methods coupled with correlation heat maps and protein interaction networks, we observed distinct conformational changes associated with receptor agonism or antagonism. In the case of the agonist, a sequential series of movements was observed, initiating with *p*-TA distancing from ECL2, followed by TM5 and TM6 motions, culminating in the movement of ICL3 toward the carboxy terminus of hTAAR1 (as depicted in Figure 6). Conversely, the movement of ICL3 was not apparent toward CTD in the presence of the antagonist. Nonetheless, it was determined that both EPPTB and RTI hold the capacity to energetically stabilize the receptor structure even more effectively than the agonist (in the absence of the Gs structure).

These findings carry substantial structural implications for our comprehension of hTAAR1 and the actions of agonists or antagonists at GPCRs.

METHODS

Generation of the Ligand Structure. *p*-Tyramine or 4-hydroxyphenylethylamine (*p*-TA), *N*-(3-ethoxyphenyl)-4-pyrrolidin-1-yl-3-trifluoromethylbenzamide (EPPTB), and 2-[[6-(4-chlorophenyl)-3-cyano-4-(trifluoromethyl)-2-pyridinyl]-thio]-*N*-2-pyrimidinylacetamide (RTI-7470-44, hereinafter RTI) structures were generated and then energetically optimized using the Hartree−Fock level of theory and 6-31G* basis set using Spartan'18.[18]

Receptor Structure. The hTAAR1 homology model was obtained using the crystal structures of the β2AR available from the Protein Data Bank[19] (PDBid: 2RH1). This template was chosen using the following criteria: (1) the highest possible resolution of the three-dimensional description; (2) the availability of the intra- and extracellular loop structure; and (3) the degree of similarity of the residues of the BC. Using the MODELLER9v632[20] program, 100 runs were performed using standard parameters. The results were ranked based on the internal scoring function of the program. Next, analysis of geometry, stereochemistry, and energy was performed using the PROSAII server[21] and Procheck server.[22]

Complex Receptor/ligand. In order to obtain the hTAAR1/*p*-TA, hTAAR1/EPPTB, and hTAAR1/RTI complexes, molecular docking was performed using the AutoDock4.0[23] suite. A grid box of 40 × 40 × 40 with a spacing of 0.375 Å was used. The final complexes were selected based on the lowest energy and the highest probability according to the scoring function of the program.

Molecular Dynamics Simulation. The all-atom molecular dynamics (MD) studies were carried out using the coordinates obtained from the docking studies. *p*-TA, EPPTB, and RTI parameters were obtained using the antechamber in the LEaP module of AmberTools. The Amber18 suite[24] with the GAFF force field[25] ff14SB force field for proteins and LIPID14 force field for lipids[26] generates the parameters and coordinates for the simulation of complexes. Each system was inserted into a 1-palmitoyl-2-oleoyl-*sn*-glycero-3-phosphoethanolamine (POPE) membrane using Membrane Buildermodule in Charmm-Gui.[27] Each complex was solvated in a periodic box using TIP3P explicit water molecules,[28,29] and the final systems were neutralized with ions (Na^+ or Cl^-). We performed six minimization steps during which the systems were heated to 300 K using a time step of 1 fs. The minimization force constant automatically decreased by 100 in each step, starting from 500 in the first cycle to 100 in the last cycle. Subsequently, we conducted five cycles of equilibration with force constants of 500, 300, 100, 50, and 5. We employed the Langevin thermostat and Berendsen barostat for the equilibration steps in the NVT ensemble. MD simulations were carried out during 1500 ns for hTAAR1/*p*-TA, hTAAR1/EPPTB, and hTAAR1/RTI in Amber18 with the NPT ensemble for production and a time step of 2 fs. 1 atm pressure was used, and the temperature was established at 310 K; the Langevin thermostat and Berendsen barostat were used. Finally, MM-PBSA[30] studies were carried out to estimate each ligand's final binding energy to hTAAR1.

For coarse-grained molecular dynamics (CGMD), we utilized Amber18 in conjunction with the GAFF and SIRAH force fields. Protein and lipid structures in the SIRAH format were obtained using cgconv.pl from SIRAH tools.[31−33] The system was then solvated within a periodic box using WT4 explicit water molecules.[34] To achieve system neutrality, NaW + and ClW- ions were added. Finally, parameters and coordinates in the. inpcrd and. prmtop formats were obtained, and the same equilibration and production protocol as previously described was applied.

In both all-atom and coarse-grained simulations, we calculated the root mean square deviation (RMSD) for the backbone atoms with respect to their positions at the reference structure (t = 0) by using the VMD RMSD Trajectory Tool.

https://doi.org/10.1021/acsomega.3c06315
ACS Omega 2023, 8, 43051−43059

Root mean square fluctuation (RMSF) for the Cα atom of each residue was calculated separately for each simulation set using the tk console in VMD. Additionally, we obtained the solvent-accessible surface area (SASA) and radius of gyration using the same procedure as RMSF.

Protein−Protein Docking. The three-component complex hTAAR1/ligand/Gα was constructed from an equilibrated conformation of hTAAR1/*p*-TA (600 ns). The α subunit of the Gs protein was obtained from the Protein Data Bank (PDBid: 1GG2), and docking studies were carried out using the ClusPro server.[35] Using the methodology described above, MD studies were carried out using the Amber18 program.

Correlation Maps. Distances between transmembrane domains along the molecular dynamics were obtained using the VMD program.[36] An intracellular horizontal plane was established to measure the distances between TMDs from the α-atom carbons closest to the intracellular plane. These data were processed in the Orange3 program[37] by nonparametric correlation analysis using Spearman's correlation with a 95% confidence interval.

Interaction Network Analysis. The interaction analysis of the complexes under study was performed using the frame of the complexes stabilized at 1500 ns. The *.json* files were obtained using the RING server.[38] The files were analyzed in Cytoscape software v3.10.0.[39] The networks were identified by selecting amino acids from the binding cavity identified for *p*-TA (Y200, F199, F195, and F186) and intracellular loop 3 (ICL3) (L215 and K245). From these amino acids, immediate neighboring residues in the interaction network were selected and filtered to identify the largest networks.

■ ASSOCIATED CONTENT

Supporting Information

The Supporting Information is available free of charge at https://pubs.acs.org/doi/10.1021/acsomega.3c06315.

Structural analysis of molecular dynamics of complexes hTAAR1 with the agonist and antagonists, description of hTAAR1 conformational changes from molecular dynamics, and interaction network of hTAAR1/ligands (PDF)

■ AUTHOR INFORMATION

Corresponding Author

Angélica Fierro − *Departamento de Química Orgánica, Escuela de Química, Facultad de Química y de Farmacia, Pontificia Universidad Católica de Chile, Santiago 7820436, Chile;* orcid.org/0000-0002-6507-4188; Phone: +56223541171; Email: afierroh@uc.cl

Authors

Agustín I. Robles − *Departamento de Química Orgánica, Escuela de Química, Facultad de Química y de Farmacia, Pontificia Universidad Católica de Chile, Santiago 7820436, Chile; Department of Molecular Pharmacology & Neuroscience, Stritch School of Medicine, Loyola University Chicago, Maywood, Illinois 60611-2001, United States*

Luis Dinamarca-Villarroel − *Departamento de Química Orgánica, Escuela de Química, Facultad de Química y de Farmacia, Pontificia Universidad Católica de Chile, Santiago 7820436, Chile; Department of Molecular Pharmacology & Neuroscience, Stritch School of Medicine, Loyola University Chicago, Maywood, Illinois 60611-2001, United States*

Gonzalo E. Torres − *Department of Molecular Pharmacology & Neuroscience, Stritch School of Medicine, Loyola University Chicago, Maywood, Illinois 60611-2001, United States*

Complete contact information is available at: https://pubs.acs.org/10.1021/acsomega.3c06315

Author Contributions

A.I.R. and L.D.-V. performed molecular dynamics studies and data analysis. A.I.R., G.E.T., and A.F. designed the research project. All authors discussed the results and contributed to the final article.

Funding

This work was supported by Fondecyt 1161375 and 1221030. A.I.R. and L.D.-V. are supported by a VRI-UC and ANID 2120133 Doctoral fellowship, respectively.

Notes

The authors declare no competing financial interest.

■ ACKNOWLEDGMENTS

The authors are grateful to the Fierro and Torres laboratories for their insightful discussions.

■ ABBREVIATIONS

GPCR, G protein-coupled receptor; MD, molecular dynamics; TAAR1, trace amine-associated receptor 1

■ REFERENCES

(1) Macalino, S. J. Y.; Gosu, V.; Hong, S.; Choi, S. Role of computer-aided drug design in modern drug discovery. *Arch. Pharm. Res.* **2015**, *38*, 1686−1701.

(2) Bian, Y.; Xie, X.-Q. Computational Fragment-Based Drug Design: Current Trends, Strategies, and Applications. *AAPS J.* **2018**, *20*, No. 59.

(3) Guner, O.; Bowen, J. Pharmacophore Modeling for ADME. *Curr. Top. Med. Chem.* **2013**, *13*, 1327−1342.

(4) Yang, S. Y. Pharmacophore modeling and applications in drug discovery: Challenges and recent advances. *Drug Discovery Today.* **2010**, *15*, 444−450.

(5) Jacobson, K. A. New paradigms in GPCR drug discovery. *Biochem. Pharmacol.* **2015**, *98*, 541−555.

(6) Congreve, M.; De Graaf, C.; Swain, N. A.; Tate, C. G. Impact of GPCR Structures on Drug Discovery. *Cell* **2020**, *181*, 81−91.

(7) Dror, R. O.; Arlow, D. H.; Maragakis, P.; Mildorf, T. J.; Pan, A. C.; Xu, H.; Borhani, D. W.; Shaw, D. E. Activation mechanism of the β 2-adrenergic receptor. *Proc. Natl. Acad. Sci. U.S.A.* **2011**, *108*, 18684−18689.

(8) Mozumder, S.; Bej, A.; Sengupta, J. Ligand-Dependent Modulation of the Dynamics of Intracellular Loops Dictates Functional Selectivity of 5-HT2AR. *J. Chem. Inf. Model.* **2022**, *62*, 2522−2537.

(9) Li, J.; Remington, J. M.; Liao, C.; Parsons, R. L.; Schneebeli, S.; Braas, K. M.; May, V.; Brewer, M. GPCR Intracellular Loop Regulation of Beta-Arrestin-Mediated Endosomal Signaling Dynamics. *J. Mol. Neurosci.* **2022**, *72*, 1358−1373.

(10) Shen, C.; Mao, C.; Xu, C.; Jin, N.; Zhang, H.; Shen, D.-D.; Shen, Q.; Wang, X.; Hou, T.; Chen, Z.; Rondard, P.; Pin, J.-P.; Zhang, Y.; Liu, J. Structural basis of GABAB receptor−Gi protein coupling. *Nature* **2021**, *594*, 594−598.

(11) Borowsky, B.; Adham, N.; Jones, K. A.; Raddatz, R.; Artymyshyn, R.; Ogozalek, K. L.; Durkin, M. M.; Lakhlani, P. P.; Bonini, J. A.; Pathirana, S.; Boyle, N.; Pu, X.; Kouranova, E.; Lichtblau, H.; Ochoa, F. Y.; Branchek, T. A.; Gerald, C. Trace amines: Identification of a family of mammalian G protein-coupled receptors. *Proc. Natl. Acad. Sci. U.S.A.* **2001**, *98*, 8966−8971.

(12) Heffernan, M. L. R.; Herman, L. W.; Brown, S.; Jones, P. G.; Shao, L.; Hewitt, M. C.; Campbell, J. E.; Dedic, N.; Hopkins, S. C.; Koblan, K. S.; Xie, L. Ulotaront: A TAAR1 Agonist for the Treatment of Schizophrenia. *ACS Med. Chem. Lett.* **2022**, *13*, 92−98.
(13) Liao, S.; Pino, M. J.; Deleon, C.; Lindner-Jackson, M.; Wu, C. Interaction analyses of hTAAR1 and mTAAR1 with antagonist EPPTB. *Life Sci.* **2022**, *300*, No. 120553.
(14) Cichero, E.; Espinoza, S.; Gainetdinov, R. R.; Brasili, L.; Fossa, P. Insights into the Structure and Pharmacology of the Human Trace Amine-Associated Receptor 1 (hTAAR1): Homology Modelling and Docking Studies. *Chem. Biol. Drug Des.* **2013**, *81*, 509−516.
(15) Bradaia, A.; Trube, G.; Stalder, H.; Norcross, R. D.; Ozmen, L.; Wettstein, J. G.; Pinard, A.; Buchy, D.; Gassman, M.; Hoener, M. C.; Bettler, B. The selective antagonist EPPTB reveals TAAR1-mediated regulatory mechanisms in dopaminergic neurons of the mesolimbic system. *Proc. Natl. Acad. Sci. U.S.A.* **2009**, *106*, 20081−20086.
(16) Decker, A. M.; Brackeen, M. F.; Mohammadkhani, A.; Kormos, C. M.; Hesk, D.; Borgland, S. L.; Blough, B. E. Identification of a Potent Human Trace Amine-Associated Receptor 1 Antagonist. *ACS Chem. Neurosci.* **2022**, *13*, 1082−1095.
(17) Cherezov, V.; Rosenbaum, D. M.; Hanson, M. A.; Rasmussen, S. G. F.; Thian, F. S.; Kobilka, T. S.; Choi, H.-J.; Kuhn, P.; Weis, W. I.; Kobilka, B. K.; Stevens, R. C. High-Resolution Crystal Structure of an Engineered Human β. *Science* **2007**, *318*, 1258−1265.
(18) *Spartan'18*, version 1.4.8.; Wavefunction Inc: Irvine, CA, 2018.
(19) Berman, H. M.; Westbrook, J.; Feng, Z.; Gilliland, G.; Bhat, T. N.; Weissig, H.; Shindyalov, I. N.; Bourne, P. E. The Protein Data Bank. *Nucleic Acids Res.* **2000**, *28*, 235−242.
(20) Sali, A.; Blundell, T. L. Comparative protein modelling by satisfaction of spatial restrains. *J. Mol. Biol.* **1993**, *234*, 779−815.
(21) Wiederstein, M.; Sippl, M. J. ProSA-web: Interactive web service for the recognition of errors in three-dimensional structures of proteins. *Nucleic Acids Res.* **2007**, *35*, W407−W410.
(22) Laskowski, R. A.; MacArthur, M. W.; Moss, D. S.; Thornton, J. M. PROCHECK: a program to check the stereochemical quality of protein structures. *J. Appl. Crystallogr.* **1993**, *26*, 283−291.
(23) Morris, G. M.; Goodsell, D. S.; Halliday, R. S.; Huey, R.; Hart, W. E.; Belew, R. K.; Olson, A. J. Automated docking using a Lamarckian genetic algorithm and an empirical binding free energy function. *J. Comput. Chem.* **1998**, *19*, 1639−1662.
(24) Salomon-Ferrer, R.; Case, D. A.; Walker, R. C. An overview of the Amber biomolecular simulation package. *Wiley Interdiscip. Rev.: Comput. Mol. Sci.* **2013**, *3*, 198−210.
(25) Ponder, J. W.; Case, D. A. Force Fields for Protein Simulations. In *Advances in Protein Chemistry*; Dagget, V., Ed.; Academic Press, 2003; Vol. *66*, pp 27−85.
(26) Dickson, C. J.; Madej, B. D.; Skjevik, A. A.; Betz, R. M.; Teigen, K.; Gould, I. R.; Walker, R. C. Lipid14: The Amber Lipid Force Field. *J. Chem. Theory Comput.* **2014**, *10*, 865−879.
(27) Jo, S.; Kim, T.; Iyer, V. G.; Im, W. CHARMM-GUI: A Web-Based Graphical User Interface for CHARMM. *J. Comput. Chem.* **2008**, *29*, 1859−1865.
(28) Jorgensen, W. L.; Chandrasekhar, J.; Madura, J. D.; Impey, R. W.; Klein, M. L. Comparison of simple potential functions for simulating liquid water. *J. Chem. Phys.* **1983**, *79*, 926−935.
(29) Mark, P.; Nilsson, L. Structure and Dynamics of the TIP3P, SPC, and SPC/E Water Models at 298 K. *J. Phys. Chem. A* **2001**, *105*, 9954−9960.
(30) Kollman, P. A.; Massova, I.; Reyes, C.; Kuhn, B.; Huo, S.; Chong, L.; Lee, M.; Lee, T.; Duan, Y.; Wang, W.; Donini, O.; Cieplak, P.; Srinivasan, J.; Case, D. A.; Cheatham, T. E. Calculating Structures and Free Energies of Complex Molecules: Combining Molecular Mechanics and Continuum Models. *Acc. Chem. Res.* **2000**, *33*, 889−897.
(31) Machado, M. R.; Barrera, E. E.; Klein, F.; Sóñora, M.; Silva, S.; Pantano, S. The SIRAH 2.0 Force Field: Altius, Fortius, Citius. *J. Chem. Theory Comput.* **2019**, *15*, 2719−2733.
(32) Machado, M. R.; Pantano, S. SIRAH tools: mapping, backmapping and visualization of coarse-grained models. *Bioinformatics* **2016**, *32*, 1568−1570.
(33) Barrera, E. E.; Machado, M. R.; Pantano, S. J. Fat SIRAH: Coarse-Grained Phospholipids To Explore Membrane−Protein Dynamics. *J. Chem. Theory Comput.* **2019**, *15*, 5674−5688.
(34) Darré, L.; Machado, M. R.; Dans, P. D.; Herrera, F. E.; Pantano, S. Another Coarse Grain Model for Aqueous Solvation:-WAT FOUR? *J. Chem. Theory Comput.* **2010**, *6*, 3793−3807.
(35) Kozakov, D.; Hall, D. R.; Xia, B.; Porter, K. A.; Padhorny, D.; Yueh, C.; Beglov, D.; Vajda, S. The ClusPro web server for protein−protein docking. *Nat. Protoc.* **2017**, *12*, 255−278.
(36) Humphrey, W.; Dalke, A.; Schulten, K. VMD: Visual molecular dynamics. *J. Mol. Graphics* **1996**, *14*, 33−38.
(37) Demsar, J.; Curk, T.; Erjavec, A.; Gorup, C.; Hocevar, T.; Milutinovic, M.; Mozina, M.; Polajnar, M.; Toplak, M.; Staric, A.; Stajdohar, M.; Umek, L.; Zagar, L.; Zbontar, J.; Zitnik, M.; Zupan, B. Orange: Data Mining Toolbox in Python. *J. Mach. Learn. Res.* **2013**, *14*, 2349−2353.
(38) Clementel, D.; Del Conte, A.; Monzon, A. M.; Camagni, G. F.; Minervini, G.; Piovesan, D.; Tosatto, S. C. E. RING 3.0: fast generation of probabilistic residue interaction networks from structural ensembles. *Nucleic Acids Res.* **2022**, *50*, W651−W656.
(39) Shannon, P.; Markiel, A.; Ozier, O.; Baliga, N. S.; Wang, J. T.; Ramage, D.; Amin, N.; Schwikowski, B.; Ideker, T. Cytoscape: A Software Environment for Integrated Models of Biomolecular Interaction Networks. *Genomes Res.* **2003**, *13*, 2498−2504.

NOTE ADDED AFTER ASAP PUBLICATION

This paper originally published ASAP on October 31, 2023. As Figures 3 and 4 were identical, a corrected version was reposted on November 1, 2023.

https://doi.org/10.1021/acsomega.3c06315
ACS Omega 2023, 8, 43051−43059